Mineralogical Magazine, November 2015, Vol. 79(6), pp. 1455–1466

OPEN ACCESS

Radiation damage from long-term alpha particle bombardment of silicates – a microfocus XRD and Fe *K*-edge XANES study

W. R. Bower[1,*], C. I. Pearce[2], G. T. R. Droop[1], J. F. W. Mosselmans[3], K. Geraki[3] and R. A. D. Pattrick[1]

[1] Research Centre for Radwaste Disposal and Williamson Research Centre, School of Earth, Atmospheric and Environmental Sciences, The University of Manchester M13 9PL, UK
[2] Dalton Nuclear Institute & School of Chemistry, The University of Manchester M13 9PL, UK
[3] Diamond Light Source, Harwell OX11 0QX, UK

[*Received 17 October 2014; Accepted 6 June 2015; Associate Editor: Nicholas Evans*]

ABSTRACT

A detailed understanding of the response of mineral phases to the radiation fields experienced in a geological disposal facility (GDF) is currently poorly constrained. Prolongued ion irradiation has the potential to affect both the physical integrity and oxidation state of materials and therefore may alter a structure's ability to react with radionuclides. Radiohalos (spheres of radiation damage in minerals surrounding radioactive (α-emitting) inclusions) provide useful analogues for studying long term α-particle damage accumulation. In this study, silicate minerals adjacent to Th- and U-rich monazite and zircon were probed for redox changes and long/short range disorder using microfocus X-ray absorption spectroscopy (XAS) and high resolution X-ray diffraction (XRD) at Beamline I18, Diamond Light Source. $Fe^{3+} \rightarrow Fe^{2+}$ reduction has been demonstrated in an amphibole sample containing structural OH^- groups – a trend not observed in anhydrous phases such as garnet. Coincident with the findings of Pattrick *et al.* (2013), the radiolytic breakdown of OH^- groups is postulated to liberate Fe^{3+} reducing electrons. Across all samples, high point defect densities and minor lattice aberrations are apparent adjacent to the radioactive inclusion, demonstrated by micro-XRD.

Keywords: radiation damage, alpha particle, silicates, Fe *K*-edge, XRD, XANES.

Introduction

With the majority of the global stockpiles of radioactive waste destined for long-term (>100,000 years) isolation in a deep geological disposal facility (GDF), a critical understanding of the mechanisms and consequences of radiation damage across mineral phases is essential for building a safety case. Regardless of lithology, the host rock will be expected to act as the final barrier towards radionuclide migration following eventual waste canister failure (NDA, 2010*a,b*) and radiation damage will occur where escaping radionuclides accumulate. Additionally, the performance assessment of near-field barrier materials (i.e. bentonite backfill, cements, etc.) and the wasteforms themselves employed in a GDF will be aided by detailed studies of radiation damage effects in minerals (Ewing, 2001). Natural mineral assemblages containing radioactive inclusions provide useful proxies for the response of silicate phases to prolongued α-irradiation. Aureoles of radiation

* E-mail: william.bower@manchester.ac.uk
DOI: 10.1180/minmag.2015.079.6.20

The publication of this research has been funded by the European Union's European Atomic Energy Community's (Euratom) Seventh Framework programme FP7 (2007–2013) under grant agreements n°249396, SecIGD, and n°323260, SecIGD2.

damage ($r = \sim$30–50 μm) form in minerals that surround α-particle emitting inclusions [e.g. Th-rich monazite ($CePO_4$), U-rich zircon ($ZrSiO_4$)], resulting from the high-energy α-particles ($^4He^{2+}$ ions) penetrating into the neighbouring crystal and causing hundreds of atomic displacements at the end of their projected range. An α-particle will lose most of its energy via ionization of the structure through which it penetrates, eventually resulting in a concentration of Frenkel (interstitial) defect accumulation following sufficient energy loss. Ionization effects (such as electron holes and consequent charge imbalances) are likely to anneal or recombine through time, whilst the more enduring structural defects can remain for millions of years (Nasdala *et al.*, 2001, 2006). Petrographically termed 'radiohalos', silicate minerals commonly exhibit marked discolouration across an irradiated area as a result of the accumulation of these point defects and ionization effects.

Prior studies into the extent of structural damage in radiohalos primarily include sheet silicates such as biotite mica and chlorite; these phases often exhibit the most marked discolouration. In phyllosilicates, where the radioactive inclusions are often only a few microns across, the radiohalos are identified optically

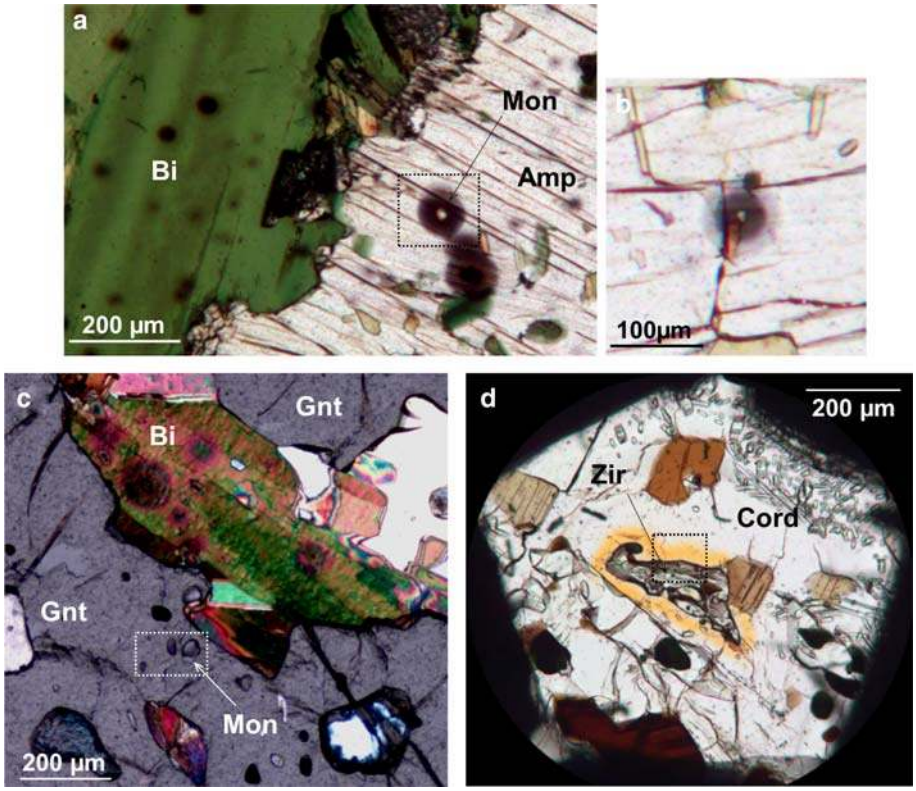

FIG. 1. (*a*) Plane-polarized optical microscope image of radiohalos in grunerite (Amp) surrounding monazite inclusions (Mon) within an almandine-grunerite-biotite (Bi) meta-ironstone from Tunaberg, Sweden. Note the dark brown, smeared discolouration surrounding the inclusion resulting from prolongued radiation damage (~1.8 Ga). (*b*) Example of a radiohalo in grunerite surrounding an inclusion of monazite, displaying an inner, darker halo surrounded by a more diffuse outer ring. (*c*) Cross-polarized optical microscope image of inclusions of monazite (also zircon) in a garnet (Gnt)-cordierite-biotite (Bi) gneiss taken from the Huntly complex, NE Scotland. Note the prominent radiohalos (~470 Ga) surrounding the monazite inclusions within the neighbouring biotite crystal, which are not visible in the garnet. (*d*) Plane-polarized optical microscope image of a pale yellow radiohalo in cordierite (Cord) surrounding an inclusion of zircon (Zir) in granulite-facies pelitic gneiss from Madagascar. Across all images, representative areas for the presented data have been marked with dashed boxes.

https://doi.org/10.1180/minmag.2015.079.6.20 Published online by Cambridge University Press

as a series of concentric darkened spheres, the diameter of each sphere (seen as circular ring in thin section) corresponding to the energy of the α-particle along the uranium/thorium decay chain (~4–8 MeV) (Demayo *et al.*, 1981; Nasdala *et al.*, 2001, 2006; Pal, 2004). If the Th/U-bearing phases are larger, the damage halo mimics the grain shape and rings become poorly defined. Radiohalos in biotite mica (Fig. 1) have been demonstrated to contain extensive loss of short-range order by α-particle bombardment

TABLE 1. Details of the minerals analysed in this study, with information on the geological provenance of the samples and the differing morphologies of the radiohalos.

Sample	General formula	Sample details	Radiohalo	α-emitter
Grunerite	$Fe_7^{2+}(Si_8O_{22})(OH)_2$	Taken from an almandine-grunerite-biotite meta-ironstone, sampled near Tunaberg, Sweden, as detailed by Pattrick *et al.*, (2013). Estimated crystallization age 1.8 Ga. No thermal disturbance since ~1500 Ma.	Dark to pale brown, smeared areas of discolouration surrounding the inclusions, *c.* 40 μm in diameter. Most of the irradiated zones are hazy; becoming more diffuse towards the outer edge of the halos, whilst some radiohalos display a more distinct outer ring that is optically paler, see Fig. 1.	Monazite (anhedral) ($CePO_4$) ~30 μm diameter
Almandine (A)	$Fe_3^{2+}Al_2(SiO_4)_3$	Taken from a garnet-cordierite-biotite gneiss from Barry Hill, Huntly in NE Scotland (Dalrymple, 1995; Droop *et al.*, 2003). SEAES rock catalogue no. 20884. Sample derived by partial melting of Dalradian metasediments by a layered basic intrusion of 'Newer' gabbro suite near the thermal peak of regional metamorphism (*c.* 470 Ma). No thermal disturbance since formation.	Neither garnet sample displays an optical damage 'halo', however for clarity the irradiated area surrounding the inclusions is referred to subsequently as the 'halo region'. Neighbouring biotites within the assemblage show prominent darkened halos, see Fig. 1.	Zircon (euhedral) ($ZrSiO_4$) ~30 μm × 45 μm
Almandine (B)	As above.	As above.	As above.	Monazite (euhedral) ~80 μm × 90 μm
Cordierite	$Mg_2Al_4Si_5O_{18}$	Taken from a spinel-sillimanite-cordierite-biotite gneiss from Ihosy, Madagascar. SEAES rock catalogue no. 15834. The rock is a 560 Ma old pelitic metasediment from the Androyan System, which underwent granulite facies regional metamorphism (Nicollet, 1990; Markl, *et al.*, 2000).	Anhedral zircons have produced radiohaloes with a morphology matching the dimensions of the emitter. The discolouration, whilst not displaying any concentric patterns, is a far lighter, pale yellow colour than the dark brown present in the amphibole. A band of cordierite directly adjacent to the zircon is paler and appears not to have suffered the same degree of discolouration, see Fig. 1.	Zircon (anhedral) ~300 μm × 100 μm

https://doi.org/10.1180/minmag.2015.079.6.20 Published online by Cambridge University Press

and the electron liberating radiolysis of structural OH^- groups has been shown to reduce Fe^{3+} within the metal-rich mineral layers (Pattrick *et al.*, 2013; Bower *et al.*, 2015). Whilst not all silicate minerals display intense discolouration with damage, subtle optical effects of radiation damage have been identified here in iron-rich garnet, cordierite and amphibole adjacent to α-emitting inclusions. The following study is a synchrotron Fe *K*-edge X-ray absorption, near-edge spectroscopy (XANES) and microfocus XRD investigation across silicate phases in the vicinity of α-emitters to examine changes in Fe oxidation state, short-range order and structural defect accumulation, respectively.

Methods

Samples

Four radiation damaged silicate samples have been analysed by synchrotron microfocus XRD and Fe *K*-edge XANES. All samples examined envelop inclusions of zircon or monazite which have emitted high energy (5–8 MeV) α-particles for at least 470 Ma and display various optical effects of the resulting radiation damage, see Fig. 1. Samples with a significant Fe content were deliberately selected for optimal Fe *K*-edge XAS resolution, which is used here as an indicator of changes in short-range order and redox reactions (Table 1).

Electron probe microanalysis (EPMA)

All major-element analyses of the silicates were undertaken by WDS-spectrometry using the Cameca SX-100 electron-microprobe at the University of Manchester. Standards are as detailed in Pattrick *et al.* (2013). Reported formulae are an average of high-totalling positions (>96%) over *n* points (*n* quoted alongside each formula). The sub-optimal cross section size of many of the radioactive inclusions yielded very low totals and consequently monazite and zircon chemistry is semi-quantitative.

Synchrotron methods

Analysis of samples on Beamline I18, Diamond Light Source, UK (Mosselmans *et al.*, 2009) was carried out as detailed in Pattrick *et al.* (2013) with the initial microfocus study of radiohalos in biotite. Both XRD and XAS data were collected as 'transects' across the irradiated region and towards the α-emitter in 6 μm steps (beam spot = 3 μm). Samples were prepared as ~20 μm 'thin' sections; radiohalos were identified optically and the wafers then positioned onto glass slides with a transmission hole below the analysis area.

Microfocus X-ray diffraction

X-ray diffraction patterns were acquired at 12 keV using a Photonic Science XDI-VHR 125 CCD and peak positions calibrated with either powdered LaB_6 or Si. Acquisition times ranged from 20 s to 1 min. 1D spectra were subsequently reduced and fitted in *Igor Pro 6.34A* (2014) using the *Nika* plug in (Ilavsky, 2012). Where possible, XRD peaks were indexed using the modelling software *Jems 6.84* (Stadelmann, 2012) or relevant ICDD index cards. Diffraction peaks across all traverses have been fitted with a combination of Voigt and (in the case of more damaged areas) Gaussian line profiles to attain more precise peak positions.

Microfocus Fe K-edge X-ray Absorption Spectroscopy (XAS)

Fe *K*-edge XANES data were collected in fluorescence mode. Data were reduced and analysed using the *Demeter* software package (Ravel and Newville, 2005). All plots displayed are background-subtracted, intensity-normalized spectra; edge positions are reported according to the initial first derivative peaks. High-resolution XANES data were collected up to 50 eV beyond the Fe *K*-edge. No pre-edge trends have been reported; however this is due to data quality and there is scope here for further study. Relative changes in first shell EXAFS fitting have been displayed where relevant to aid quantification of Fe oxidation state changes. Optimal fits are limited due to the extent of the useful XAS data. Whilst first shell EXAFS fitting at low *k* ranges (50 eV past the edge, $k = 6$) will have inadequacies in fitting, relative changes in fit results will be valid. Fit results have been presented in Supplementary Information. (deposited with the Principal Editor of Mineralogical Magazine and available at www.minersoc.org/pages/e_journals/dep_mat_mm.html)

Results

Grunerite

The amphibole studied has been assigned as grunerite; EPMA both inside and outside the halo

https://doi.org/10.1180/minmag.2015.079.6.20 Published online by Cambridge University Press

regions yielded an average composition (±0.01) of:

Outside halo:

$$\left(Fe^{2+}_{4.18}Fe^{3+}_{0.09}\right),Mg_{2.15},Mn_{0.55},Na_{0.05}Ca_{0.07},Si_{7.90}O_{22.00}(OH)_{2.00}\ (n=18)$$

Inside halo:

$$\left(Fe^{2+}_{4.18}Fe^{3+}_{0.06}\right),Mg_{2.16},Mn_{0.55},Na_{0.04}Ca_{0.07},Si_{7.90}O_{22.00}(OH)_{2.00}\ (n=15)$$

Consistent with other studies (Nasdala *et al.*, 2006; Pal, 2004; Pattrick *et al.*, 2013), no significant chemical differences were observed; however, calculating all iron as Fe^{2+} and accounting for cation excesses above 15 per formula unit (p.f.u.), relative Fe^{2+}/Fe^{3+} ratios were estimated and show a slight decrease (0.03 atoms p.f.u.) in Fe^{3+} within the irradiated region. Grunerite is the Fe-rich end member of the cummingtonite–grunerite amphibole series; a double-chain silicate with chains of silica tetrahedra (containing structural OH^{-}) bonded by metal-rich octahedra, resulting in a monoclinic structure (Deer *et al.*, 1992). The radioactive monazites in this sample, confirmed by EPMA contain ~2.5 at.% Th, the primary α-emitter. Pattrick *et al.* (2013) reported the monazite composition (±0.01 p.f.u.) as:

$$(Ce_{0.40}La_{0.22}Nd_{0.12}Pr_{0.04}Sm_{0.03}Th_{0.15}U_{0.02}Si_{0.02})PO_{4.00}$$

The XANES spectra across the grunerite radiohalo show a change in the relative white line heights of the double-peaked edge (see Fig. 2). An increase in the ratio of peak i (7127 eV) to peak ii (7131 eV) represents a higher proportion of Fe with a lower average binding energy neighbouring the monazite and suggests a reduction of a proportion of the structural Fe^{3+} with increasing proximity to the α-emitter. Work by Dyar *et al.* (2002) and Monkawa *et al*. (2006) revealed the relative changes in Fe *K*-edge XANES peak heights in amphibole represent differing $Fe^{3+}/\Sigma Fe$ ratios.

First-shell EXAFS fitting was possible beyond the absorption edge. Relative changes in octahedral Fe–O interatomic distances also suggest Fe^{3+} reduction in the halo region; an overall increase in average bond length is indicative of this process (Fig. 2*b*). The average Fe–O distance outside the radiohalo is 2.073 Å, whilst within the discoloured, irradiated region this value increases to a maximum of 2.19 Å, a consequence of a higher average signal from 6-coordinated Fe^{2+}.

XRD peak fitting across the traverse reveals extensive structural damage across the irradiated region. Figure 3 illustrates three examples of XRD peak changes as a product of accumulated α-irradiation. With the exception of reflection (202) which is isolated in 2θ space, all peaks in close proximity merge and broaden with decreasing distance to the monazite, demonstrating increasing radiation damage. In the case of reflections (281) and (312), this merging is accompanied by an overall shift of the peak position of the individual reflections to higher 2θ angles (with the exception of peak ($\bar{1}$91), which has merged to lower angles or disappeared). This shift is also observed in peak (202), but the FWHM (full width at half maximum) and overall intensity of the peak has decreased. At this resolution, most reflections expand to form overlapping peaks and closely neighbouring lattice reflections are individually lost; this is especially noticeable with reflections (201), (060) and ($\bar{2}$41).

Reflection (202) represents a series of *M*4 site cations (Fe, Mg) in-plane oblique to the tetrahedral chains. Similarly, reflection (281) links octahedral cations between chains in a similar vector, both trends indicative of a chain-parallel contraction. Large voids occur periodically along the chains in pristine amphibole, a result of the alternating orientation of the tetrahedra. It is possible that increased point defects from α-particle bombardment may cause minor structural collapse into these regions that will act as sinks for displaced atoms; the amphibole structure may be highly susceptible to loss of short-range order as a result.

Almandine

The two garnets studied yielded an average formula of (±0.01 p.f.u.):

$$\left(Fe^{2+}_{2.09}Fe^{3+}_{0.06}\right)Mg_{0.81}Ca_{0.06}Mn_{0.02}Al_{1.99}Si_{2.98}O_{12.00}\ (n=20)$$

A set of points were collected adjacent to the monazite in almandine B (±0.01 p.f.u.):

$$\left(Fe^{2+}_{2.08}Fe^{3+}_{0.07}\right)Mg_{0.81}Ca_{0.057}Mn_{0.02}Al_{1.99}Si_{2.97}O_{12.00}\ (n=15)$$

No changes in chemistry inside statistical limits were observed adjacent to the α-emitter; however in contrast to the grunerite, a slight relative increase in calculated Fe^{3+} was apparent neighbouring the monazite. This is within the error of the EPMA and not a definitive trend. Almandine garnet is an

https://doi.org/10.1180/minmag.2015.079.6.20 Published online by Cambridge University Press

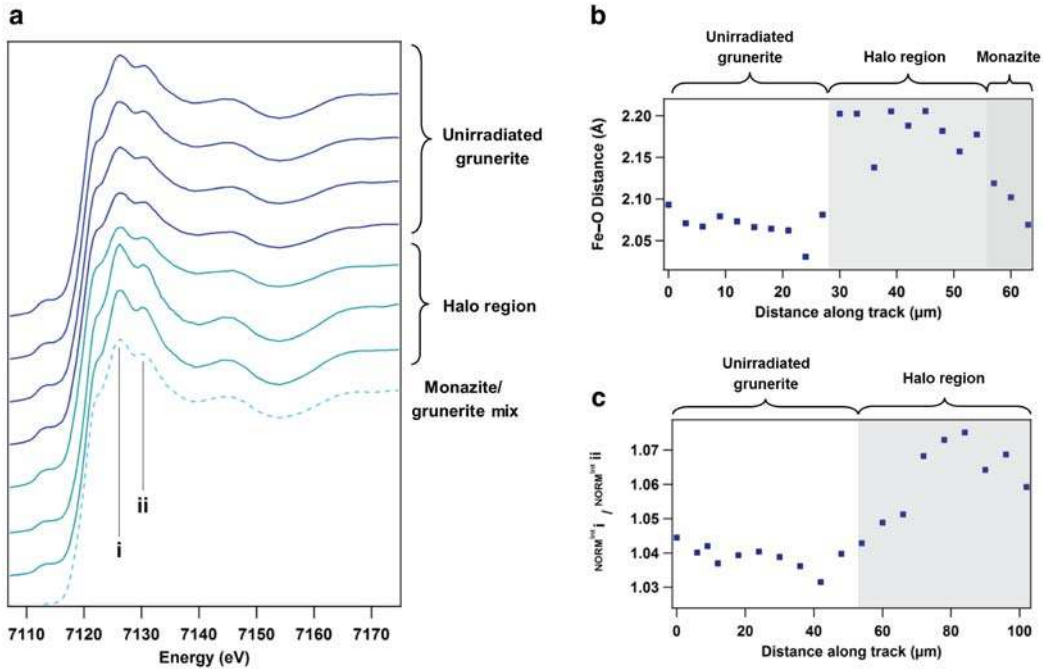

FIG. 2. (*a*) Normalized Fe *K*-edge XANES across a radiohalo in a crystal of grunerite with increasing proximity to the α-emitter (monazite). The white line is split into two peaks (~4 eV apart), interpreted as a signal from both Fe^{2+} (~7127 eV) and Fe^{3+} (~7131 eV). Within the halo, the relative intensity of peak i increases over peak ii. Spectra have been spaced for clarity; each spectrum represents a 6 µm shift along the line of traverse towards the monazite/grunerite mix (shown by a dashed line). (*b*) Absolute changes in intensities for normalized Fe *K*-edge peaks i and ii across a radiohalo transect. The increasing ratio of peak i (Fe^{2+}) to ii (Fe^{3+}) suggests a reduction of Fe^{3+} within the halo area as a product of α-particle damage. (*c*) First shell distance (Fe–O) EXAFS fit results across the XAS transect, showing an overall increase in bond lengths in the irradiated halo region. More detailed fit data are included in Supplementary Information (deposited at www.minersoc.org/pages/e_journals/dep_mat_mm.html).

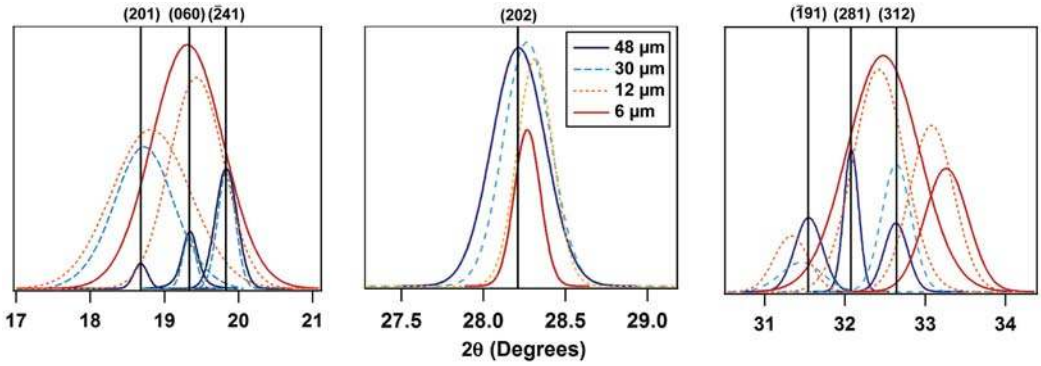

FIG. 3. Representative, fitted XRD peaks displayed at intervals along the grunerite → monazite transect. Legend denotes distances from the α-emitter. At ~35 µm, the edge of the radiohalo is approached, thus reflections at 48 µm are assumed to represent unirradiated crystal. Indexed reflections are shown above undamaged peaks where identification was possible. Note the different 2θ scales.

https://doi.org/10.1180/minmag.2015.079.6.20 Published online by Cambridge University Press

Fe-rich member of the pyrope(Mg)-almandine(Fe)-spesssartine(Mn) series; its structure consists of an orthosilicate framework of tetrahedrally and octahedrally coordinated cations, with the addition of central domains containing dominantly Fe cations surrounded by eight oxygens (Deer *et al.*, 1992). The monazite in almandine B contains ~3.1 at.% Th, slightly higher than the amphibole sample from Tunaberg. The actinide content of the zircon in almandine A is unknown; however, it is likely to contain less uranium (the primary α-emitter) than the monazites; zircons typically contain ~0.1 at.% uranium (Cuttitta and Daniels, 1959; Kusiak *et al.*, 2009; Sano *et al.*, 2000). It is important to note the differences in size between the two α-emitters, which may account for radiation damage trends.

Radiation damage induced changes are apparent in the XANES spectra of almandine A surrounding the zircon. Two spectra are shown in Fig. 4*a,* one ~6 μm from the zircon edge and a second ~48 μm from the emitter in the unirradiated garnet. Whilst there is no optical halo to act as a reference, Monte Carlo based simulation software, the Stopping and Range of Ions in Matter (*SRIM*) (Ziegler, 2013) predicts that an 8 MeV α-particle travelling through garnet with a density of 4.19 g/cm^3 and composition shown, has a maximum range of 31 μm. This excludes energy lost upon exiting the zircon. It is assumed therefore that the point at 48 μm from the emitter is unirradiated.

An overall broadening of the modulations beyond the edge is apparent in the irradiated region in almandine A. A minor shift of the white line maximum to higher energy is apparent; however the top of the edge is relatively 'flat' and the edge itself broadens with proximity to the monazite. Such a small shift is not definitive of an Fe valence change and could represent a local, natural variation or damage induced structural disorder.

It is likely that an increase in point defect density accounts for the changes in the spectra above the edge. Farges *et al*. (1997) demonstrate a broadening of the Ti *K*-edge with decreased periodicity in Ti oxide samples, attributable to a variation in edge position on an atomic scale as a function of non-uniform absorption sites. As not all atomic path lengths will be similar across irradiated samples, broader XANES (and extended) features will result.

X-ray diffraction peak fitting across almandine A shows radiation damage induced trends similar to those observed in the grunerite sample. Almandine A adjacent to zircon displays peak broadening and overall reflection intensity reduction into the 'halo' zone (Fig. 4*b*). Reflection (233) broadens and shifts to higher 2θ angles within 6 μm of the margin of the monazite, indicative of a contraction of the cyrstal in this plane. Peak (026) splits into two broad, low-intensity peaks located either side of the original reflection position, indicative of both lattice expansion and contraction in this plane (Li *et al.*, 2004). An overall increase in FWHM across most peaks within 24 μm of the zircon is again indicative of minor structural aberrations, whilst reflections (246) and (237) are significantly diminished in intensity (Fig. 4*b*).

In contrast, almandine B presents far fewer effects of radiation damage in the XRD data. Reflection (046) displays a shift to lower reflection angles within 36 μm of the margin of the monazite (Fig. 5*b*), indicative of a very slight expansionary strain of the crystal in this plane. No peak broadening is observed. All other reflections in the traverse across almandine B displayed no changes with respect to the alpha emitter, suggesting relatively low structural change as a consequence of irradiation. A similar damping effect upon the XANES signal was observed into the halo region, although not as pronounced as the trend in almandine A. First shell EXAFS fitting was possible across the transect in almandine B, Fig. 5*a* shows a slight decrease in Fe–O distance into the 'halo' region, in contrast to the trend observed within the grunerite sample.

Whilst α-particle bombardment appears to have a similar effect regardless of emitter (U *vs.* Th), almandine A (surrounding zircon) has clearly accumulated a higher degree of radiation damage, despite a lower actinide content of the α-source. This trend is difficult to fully explain. However two factors may contribute; the inclusion size and its consequent stopping power, as well as the level of damage sustained by the host lattice; in each case the zircon may allow more α-particles to escape into the garnet.

Cordierite

The cordierite studied also showed similar chemistry across the sample (±0.01):

Outside halo:

$$\left(Mg_{1.49}Fe^{2+}_{0.56}Fe^{3+}_{0.05}Mn_{0.01}Na_{0.02}\right)Al_{3.96}Si_{5.00}O_{18.00} \quad (n=11)$$

Inside halo:

$$\left(Mg_{1.49}Fe^{2+}_{0.54}Fe^{3+}_{0.05}Mn_{0.01}Na_{0.02}\right)Al_{3.97}Si_{4.99}O_{18.00} \quad (n=11)$$

https://doi.org/10.1180/minmag.2015.079.6.20 Published online by Cambridge University Press

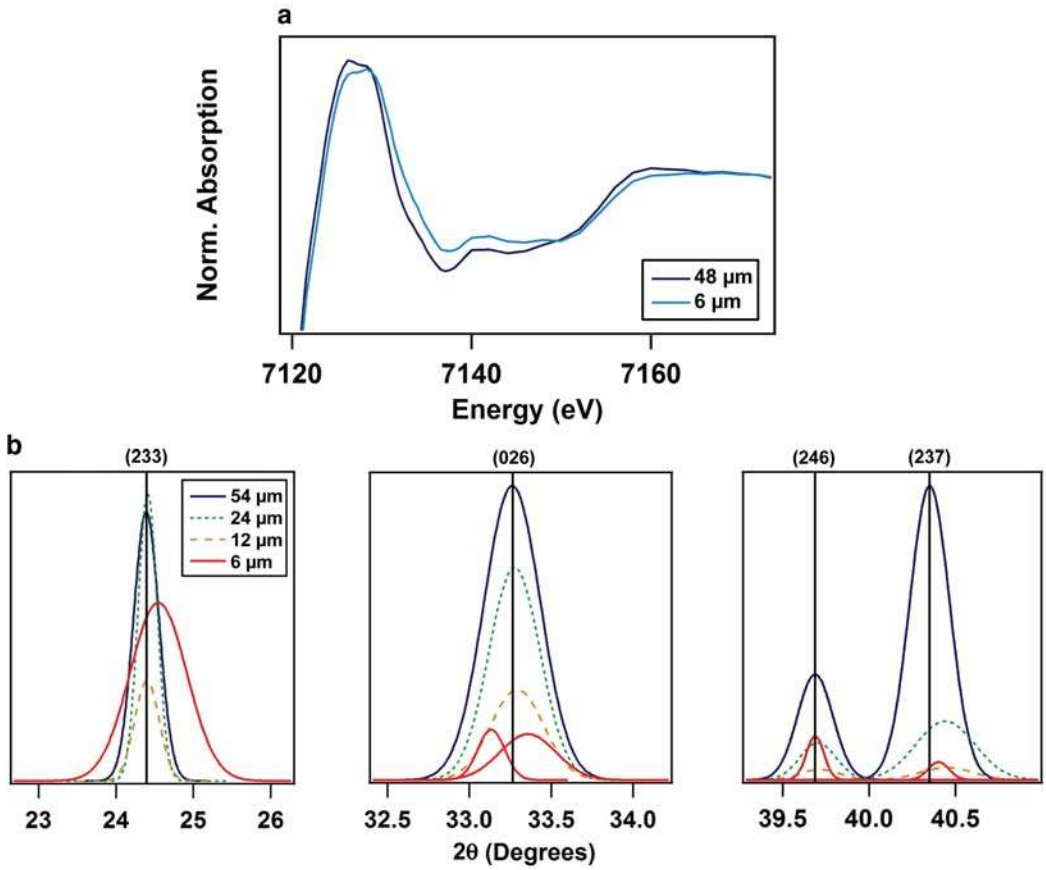

FIG. 4. (*a*) Representative Fe *K*-edge XANES spectra for almandine A both 6 µm adjacent to and 48 µm distant from an inclusion of zircon. (*b*) XRD traverse across almandine A surrounding the zircon inclusion. Assumed to have accumulated more radiation damage than almandine B, most XRD peaks across the track decrease in intensity and broaden into the irradiated region.

Cordierite is an orthorhombic (pseudohexagonal) cyclosilicate comprising a framework of six-membered tetrahedral silica/alumina rings joined laterally by further tetrahedral Al or Si as well as periodic octahedral Mg or Fe. Water molecules can be present within the rings (Rigby and Droop, 2008; Deer *et al.*, 1992). Rigby and Droop (2008) measured the volatile content of this cordierite, presenting mean values of 0.31 moles H_2O and 0.012 moles CO_2 per formula unit.

No changes were observed in the XANES transect across the cordierite radiohalo. Whilst it is likely that the cordierite has received a lower α-flux than the other samples analysed (assumed by the 'pale' discolouration intensity); the Fe content of the sample is far lower in comparison to those previously analysed; therefore redox changes may be less easily observed. The presence of a small amount of water within the structure may also be contributing to the slight colour change, not observed in anhydrous phases.

Data from points both in the pale yellow halo region and in the relatively clear band adjacent to the zircon were collected; however X-ray diffraction results did not show a trend in radiation damage coincident with the pattern of discolouration. Indeed, the highest density of point defects are neighbouring the zircon edge, demonstrated by line broadening (Fig. 6).

Discussion

This investigation has revealed the extent of radiation damage manifested in radiohalos within

https://doi.org/10.1180/minmag.2015.079.6.20 Published online by Cambridge University Press

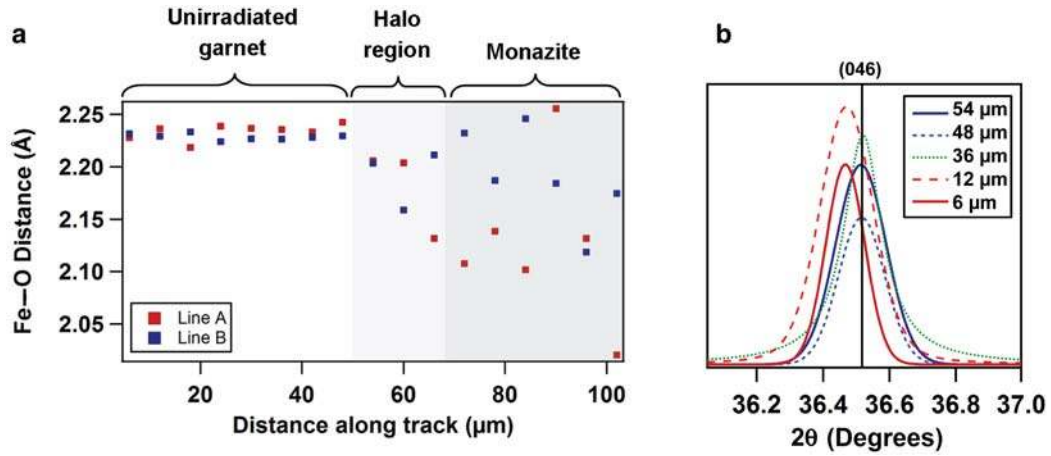

FIG. 5. (*a*) First-shell Fe–O fit results from almandine B into the monazite inclusion, showing a small shortening of bond lengths across two individual tracks. (*b*) X-ray diffraction patterns across almandine B with increasing proximity to the alpha emitter (monazite). Distances denote range from monazite surface.

a range of silicate minerals. The discolouration seen around α-emitters reflects the earliest stages of metamictization, similar to that recorded in phyllosilicates (Pal, 2004; Nasdala *et al.*, 2001, 2006; Pattrick *et al.*, 2013). Across all phases presented here, the intrinsic mineral structure is preserved within the irradiated regions (as evidenced by retention of the main XRD peak intensities and

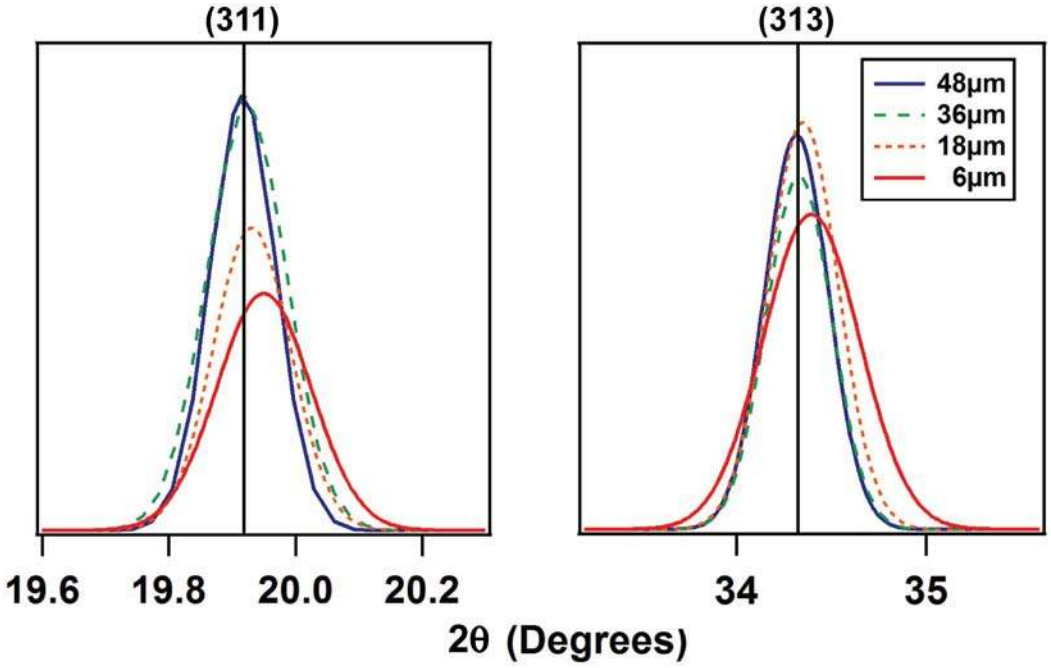

FIG. 6. XRD traverse across a radiohalo in cordierite surrounding an inclusion of zircon. Note the overall broadening of the fitted peaks within ~18 μm of the α-source; no relationship between the more intensely discoloured band and the paler region close to the zircon is observed. Note the different 2θ scales.

https://doi.org/10.1180/minmag.2015.079.6.20 Published online by Cambridge University Press

positions); however radiation damage is clearly present, to differing degrees.

Varying contributions from point (Frenkel) defect accumulation are pervasive across all radiohalos, regardless of mineral phase. Diffuse scattering (broadening of XRD peaks) is a common characteristic of low-level point defect accumulation and represents imperfections in lattice periodicity (Chailley *et al.*, 1994), with individual domains of variable defect densities existing over sub-micron scale volumes. In contrast to perfect-crystal order with sharp-peak Bragg scattering, diffuse scattering denotes non-uniform distortion along a crystal plane, thereby increasing the range of permitted diffraction angles and broadening XRD peaks. Where peaks are close in 2θ space, individual reflections merge and are lost as a product of broadening. Whilst Bragg diffraction peaks generally lose intensity with radiation damage, merging has led to some diffuse peaks apparently gaining intensity across the traverses shown here. In no instance were the samples entirely amorphous or 'metamict' (Ewing *et al.*, 1988; Tomavsić *et al.*, 2008) within the halo regions; indeed it is likely that amorphization (if any) occurs over small, discrete areas, resulting from sporadic, high concentrations of point defects. Over geological timescales, minerals may form stable clusters of defects within a broadly crystalline lattice, allowing for long-term retention of radiation damage without detriment to the overall structure (Ewing *et al.*, 2000).

Minor shifts in peak position with radiation damage are indicative of volume changes in the lattice. In the XRD patterns shown here, peaks display small movements in 2θ space, indicative of damage-induced lattice expansion and contraction on the order of +/–0.002 Å. In the instance of Frenkel defect formation, a trade-off exists between a minor volume increase (interstitial relocation) and decrease (vacancy formation and relaxation) (Grigull *et al.*, 2001). Both mechanisms appear to be present across the damaged regions identified here, with no apparent patterns across areas with higher defect densities.

Microfocus analysis suggests that the highest level of structural damage occurs directly adjacent to the α-emitter. This is in contrast with conventional models of α-particle energy deposition, whereby an α-particle creates a narrow domain of structural defects only over the final ~6 μm of its range (as predicted by SRIM) (Ziegler, 2013). This trend may be partially a factor of alpha particle energy loss before leaving the source lattice. Another possibility is the potential for a 'wandering' α-recoil effect beyond the extent of the host lattice. Upon ejecting an α-particle, the subsequent daughter nucleus will recoil (E = ~0.1 MeV) in a random direction. Multiple recoil effects along a similar vector have the potential to create a high-defect region as long as 100 nm (Seydoux-Guillaume *et al.*, 2009); this has the potential to increase over geological timescales. Nasdala *et al.* (2006) suggest the presence of a far smaller 'α-recoil halo' directly adjacent to a decaying emitter may contain extensive radiation defects.

The exact mechanism of discolouration (ionization *vs.* structural defects) across radiohalos is still a subject of debate (Nasdala *et al.*, 2006). This study finds that discolouration and structural damage do not always directly coincide; it is possible that colour-inducing radiation 'damage' may be more a product of ionization mechanisms, whilst point defects alone do not directly produce a pattern of discolouration. It should be noted that 'darkening' over irradiated areas is only present in hydrated mineral phases (biotite, chlorite, cordierite, amphibole) (Nasdala *et al.*, 2001, 2006; Pal, 2004).

Iron redox chemistry has been shown to be influenced by prolongued α-irradiation. A Fe^{3+} to Fe^{2+} reduction mechanism via the radiolysis of structural OH^{-} within α-irradiated biotite has been suggested by Pattrick *et al.* (2013); a similar trend has also been demonstrated for grunerite in this study (also containing structural hydroxyl groups within the lattice). In direct comparison, anhydrous structures such as garnet show no such trends. The presence of water within the structure appears to be a major driver of Fe redox reactions, further experimental work into which is necessary, as OH-bearing phyllosilicates are important in the near- and far-field of a GDF and the consequences of radiolytic degradation are a necessary consideration for hydraulic barriers such as bentonite.

Conclusion

Silicate minerals hosting radioactive inclusions provide useful analogues for the structural and chemical response of such phases to long-term alpha particle bombardment. Whilst radiation damage at these (unknown) doses is broadly accommodated by the structure, absorbing phases within the host rock that isolate and even incorporate actinides will suffer a degree of α-particle damage. There is potential for short-range, highly amorphizing α-recoil effects (Chakoumakos

https://doi.org/10.1180/minmag.2015.079.6.20 Published online by Cambridge University Press

et al., 1987; Meldrum *et al.*, 1998; Weber *et al.*, 1994). Increased defect densities and consequent structural accommodation/phase changes may affect mineral properties and behaviour, which may prove to be highly variable over micrometre (even nanometre) scale regions. Microfocus study of radiohalos is a useful tool to constrain the spatial extent of damage and its relationship to a radiation source.

Some drawbacks arise from the study of radiohalos as radiation damage proxies. The stochastic nature of α-particle damage accumulation from radioactive inclusions of differing morphologies makes direct comparison between (and within) halos difficult. More generally, all studies of naturally accumulated radiation effects must take into account the thermal history of the sample; however this is not a critical issue in the samples analysed here. Analysis of radiohalos yields overall, time-averaged trends resulting from an exceptionally long timescale of defect accumulation and natural crystal relaxation/defect stabilization must be considered.

Despite the advantages of studying long-term radiation damage accumulation in radiohalos, a critical concern for durability and performance studies is the need to accurately constrain doses and dose rates across irradiated materials. The α-dose rate across radiohalos is likely to be extremely low, such that recombination of defects or lattice stabilization is accommodated despite prolonged irradiation; however damage accumulation adjacent to an emitter appears far more lasting. There is doubtless a structure effect on lattice susceptibility to radiation damage; whilst direct radiation dose comparisons cannot be made, the amphibole studied here displays the highest degree of structural discontinuity in comparison to the likely more robust, isotropic silicate frameworks of the garnet. Significant further work with controlled α-irradiations is required to determine the effect of lattice structure upon damage manifestation.

Acknowledgements

WRB acknowledges the support of a NERC DTA award at the University of Manchester (NE/K500859/1) and we are grateful to Diamond Light Source for access to beamline I18 (beamtime awards SP585 SP9044). Steve Stockley is thanked for prepartion of the rock samples. The overarching support of the Research Centre for Radwaste Disposal (RCRD), University of Manchester, is gratefully acknowledged.

References

Bower, W.R., Pattrick, R.A.D., Pearce, C.I., Droop, G.T.R. and Haigh, S.J. (2015) Radiation damage halos in biotite investigated using high resolution transmission electron microscopy. *American Mineralogist*, **100** (in press).

Chailley, V., Dooryhée, E., Bouffard, S., Balanzat, E. and Levalois, M. (1994) Observations by X-ray diffraction of structural changes in mica irradiated by swift heavy ions. Pp. 162–167 in: *Nuclear Instruments and Methods in Physics Research Section B: Beam Interactions with Materials and Atoms.* Article 91.

Chakoumakos, B.C. Murakami, T. Lumpkin, G.R. and Ewing, R.C. (1987) Alpha decay induced fracturing in zircon: the transition from the crystalline to the metamict state. *Science*, **236**, 1556–1559.

Cuttitta, F. and Daniels, G.J. (1959) Determination of uranium in zircon. *Analitica Chimica Acta*, **20**, 430–434.

Dalyrimple, D.J. (1995) *Contact Anatexis of Dalradian Metapelites from the Huntly-Knock area, Aberdeenshire, Scotland.* PhD Thesis. University of Manchester, UK.

Deer, W.A. Howie, R.A. and Zussman, J. (1992) *An Introduction to the Rock Forming Minerals*, Second. Edition. Longman Scientific and Technical.

Demayo, B., Seal, M. and Vance, E.R. (1981) Optical spectra of giant radiohaloes in Madagascan biotite. *American Mineralogist*, **66**, 358–361.

Droop, G.T.R. Clemens, D.J. and Dalyrimple, D.J. (2003) Processes and conditions during contact anatexis, melt escape and restite formation: the Huntly Gabbro Complex, NE Scotland. *Journal of Petrology*, **44**, 995–1029.

Dyar, M.D., Gunter, M.E., Delaney, J.S., Lanzarotti, A. and Sutton, S.R. (2002) Systematics in the structure and XANES spectra of pyroxenes, amphiboles and micas as derived from oriented single crystals. *The Canadian Mineralogist*, **40**, 1375–1393.

Ewing, R.C. (2001) The design and evaluation of nuclear-waste forms: clues from mineralogy. *The Canadian Mineralogist*, **39**, 697–715.

Ewing, R.C. Lytle, F.W. Greegor, R.B. Murakami, T. Lumpkin, G.R. and Chakoumakos, B.C. (1988) Metamict minerals – natural analogues for radiation damage effects in ceramic nuclear waste forms. *Nuclear Instruments and Methods in Physics Research*, **B32**, 487–497.

Ewing, R.C., Meldrum, A., Wang, L. and Wang, S. (2000) Radiation-induced amorphization. Pp. 319–361 in: *Transformation Processes in Minerals* (S.A. T. Redfern and M.A. Carpenter, editors). Reviews in Mineralogy and Geochemistry, **39**. Mineralogical Society of America and the Geochemical Society, Washington, DC.

https://doi.org/10.1180/minmag.2015.079.6.20 Published online by Cambridge University Press

Farges, F., Brown, G.E., jr. and Rehr, J.J. (1997) Ti K-edge XANES studies of Ti coordination and disorder in oxide compounds: Comparison between theory and experiment. *Physical Review*, **B56**, 1809–1819.

Grigull, S., Ishimaru, M., Nastasi, M., Zorman, C.A. and Mehregany, M. (2001) In situ X-ray diffraction analysis of disorder and strain in ion implanted ceramic thin films. *ICDD Advancements in X-Ray Analysis*, **44**, 308–313.

Igor Pro (2014) WaveMetrics, Inc., Oregon, USA.

Ilavsky, J. (2012) Nika – software for 2D data reduction. *Journal of Applied Crystallography*, **45**, 324–328.

Kusiak, M.A., Dunkley, D.J., Slaby, E., Martin, H. and Budzyn, B. (2009) Sensitive high-resolution ion microprobe analysis of zircon reequilibrated by late magmatic fluids in a hybridized pluton. *Geology*, **37**, 1063–1066.

Li, J., Wu, X., Hu, D., Yang, Y., Qiu, T. and Shen, J. (2004) Splitting of X-ray diffraction peak in (Ge:SiO_2)/SiO_2 multilayers. *Solid State Communications*, **131**, 21–25.

Markl, G., Bauerle, J. and Grujie, D. (2000) Metamorphic evolution of pan-African granulite facies metapelites from southern Madagascar. *Precambrian Research*, **102**, 47–68.

Meldrum, A., Boatner, L.A., Weber, W.J. and Ewing, R.C. (1998) Radiation damage in zircon and monazite. *Geochimica et Cosmochimica Acta*, **62**, 2509–2520.

Monkawa, A., Mikouchi, T., Koizumi, E., Sugiyama, K. and Miyamoto, M. (2006) Determination of the Fe oxidation state of the Chassigny kaersutite: A microXANES spectroscopic study. *Meteoritics and Planetary Science*, **41**, 1321–1329.

Mosselmans, J.F.W., Quinn, P.D., Dent, A.J., Cavill, S.A., Moreno, S.D., Peach, A., Leicester, P.J., Keylock, S.J., Gregory, S.R., Atkinson, K.D. and Rosell, J.R. (2009) I18 – the microfocus spectroscopy beamline at the Diamond Light Source. *J. Synchrotron Radiation*, **16**, 818–824.

Nasdala, L., Wenzel, M., Andrut, M., Wirth, R. and Blaum, P. (2001) The nature of radiohaloes in biotite: Experimental studies and modeling. *American Mineralogist*, **86**, 498–512.

Nasdala, L., Wildner, M., Wirth, R., Groschopf, N., Pal, D.C. and Möller, A. (2006) Alpha particle haloes in chlorite and cordierite. *Mineralogy and Petrology*, **86**, 1–27.

NDA [Nuclear Decommissioning Authority] (2010*a*) *Geological Disposal: Steps Towards Implementation* (No. NDA/RWMD/013).

NDA [Nuclear Decommissioning Authority] (2010*b*) *Geological Disposal: Generic Disposal System Functional Specification* (No. NDA/RWMD/043).

Nicollet, C. (1990) Occurences of grandidierite, serendibite and tourmaline near Ihosy, southern Madagascar. *Mineralogical Magazine*, **54**, 131–133.

Pal, D.C. (2004) Concentric rings of radioactive halo in chlorite, Turamdih uranium deposit, Singhbhum Shear Zone, Eastern India: a possible result of ^{238}U chain decay. *Current Science*, **87**, 662–667.

Pattrick, R.A.D., Charnock, J.M., Geraki, T., Mosselmans, J.F.W., Pearce, C.I., Pimblott, S. and Droop, G.T.R. (2013) Alpha particle damage in biotite characterised by microfocus X-ray diffraction and Fe *K*-edge X-ray absorption spectroscopy. *Mineralogical Magazine*, **77**, 2867–2882.

Ravel, B. and Newville, M. (2005) ATHENA, ARTEMIS, HEPHAESTUS: data analysis for X-ray absorption spectroscopy using IFEFFIT. *Journal of Synchrotron Radiation*, **12**, 537–541.

Rigby, M.J. and Droop, G.T.R. (2008) The cordierite fluid monitor: case studies for and against its potential application. *European Journal of Mineralogy*, **20**, 693–712.

Sano, Y., Hidaka, H., Terada, K., Shimizu, H. and Suzuki, M. (2000) Ion microprobe U-Pb zircon geochronology of the Hida gneiss: Finding of the oldest minerals in Japan. *Geochemical Journal of Japan*, **34**, 135–154.

Seydoux-Guillaume, A.-M., Montel, J.-M., Wirth, R. and Moine, B. (2009) Radiation damage in diopside and calcite crystals from uranothorianite inclusions. *Chemical Geology*, **261**, 318–332.

Stadelmann, P. (2012) Jems Electron Microscopy Software. Saas-Fee, Switzerland.

Tomavsić, N., Bermanec, V., Gajović, A., Rajić Linarić, M. (2008) Metamict minerals: an insight into a relic crystal structure using XRD, Raman Spectroscopy, SAED and HRTEM. *Croatica Chemica Acta*, **81**, 391–400.

Weber, W.J. Ewing, R.C. and Wang, L.M. (1994) The radiation-induced crystalline-to-amorphous transition in zircon. *Journal of Materials Research*, **9**, 688–698.

Ziegler, J.F. (2013) The Stopping and Range of Ions in Matter (SRIM). SRIM.org

https://doi.org/10.1180/minmag.2015.079.6.20 Published online by Cambridge University Press